Unveiling True 3D Nanoscale Microstructural Evolution in Chalcogenide Nanocomposites: A Roadmap for Advanced Infrared Functionality

Myungkoo Kang, Isabelle Martin, Rashi Sharma, Cesar Blanco, Stoichko Antonov, Ty J. Prosa, David J. Larson, Hugues Francois-Saint-Cyr,* and Kathleen A. Richardson*

The design of multiphase optical nanocomposites necessitates the understanding of coexisting phases' morphology and chemistry which have deterministic impacts on light–matter interaction. A prominent example is gradient refractive index (GRIN) materials proposed to realize an arbitrarily shaped, single optical component with minimal chromatic aberration. Ge-As-Pb-Se materials are promising for GRIN due to their ability to exhibit spatially varying volume fraction of high-index Pb-rich phases in low index matrices. These materials are characterized to date, exclusively using transmission electron microscopy to reveal their phase separation and induced crystalline phase(s). It is found in the study that the intrinsic 2D perspective of the technique has hindered the identification of true morphology. To clarify this ambiguity, atom probe tomography (APT) is utilized to gain the first-ever observation of the nanocomposites' microstructure and its evolution upon heat treatment in a 3D space. The APT-quantified geometry and chemistry of coexisting phases are considered to predict the effective media's optical behaviors which closely match experimental data, enabling the establishment of the material's predictive and accurate process–structure–property relationship. Findings in the study demonstrate the robustness and advantage of the APT-assisted characterization in the design and realization of GRIN materials.

1. Introduction

Next-generation optical systems will require new optical materials which exhibit robust properties, are manufacturable using cutting edge design and fabrication tools and are compatible with system integration with other materials. One way to achieve such compatibility is through composition and/or microstructure gradients which spatially change functions across radial or axial spatial directions. Gradient refractive index (GRIN) media represent one such means where such spatial tailoring of optical property variation can satisfy currently unmet needs in optical system engineering. Most notably, the reduction in the size, weight, and power consumption of optical components and resulting systems continues to be an area of intense study looking for innovative material and design strategies. A notable area where this approach has been actively sought-after is in imaging systems. Specifically, IR components based on spherical or aspherical lenses have been widely used in imaging systems but are often large and heavy due to the multiple crystalline optical components required for compensation of chromatic aberration.[1–9] Meanwhile, GRIN materials have been developed to locally tailor refractive index within a material, thereby enabling a flat or arbitrarily shaped, single optical component with minimal chromatic aberration and providing a potential solution to this challenge.[10–16] Among candidate materials for IR GRIN, Ge-As-Pb-Se chalcogenide glasses have received great interest since one can modulate refractive index through the formation of high refractive index Pb-rich nanocrystalline phases in a lower index matrix. Through control of their volume fraction within the glassy matrix upon heat treatment or laser exposure, spatial gradients can be formed while maintaining the component's IR transparency.[17–21] The glass-ceramic nanocomposite's effective refractive index can be approximated by the summation of *refractive index × volume fraction* product for induced Pb-rich nanocrystals and the residual amorphous matrix. The formulation indicates that spatial variation in the volume fraction of high refractive index nanocrystals can lead to

Dr. M. Kang, Dr. R. Sharma, C. Blanco, Prof. K. A. Richardson
CREOL
College of Optics and Photonics
University of Central Florida
Orlando, FL 32816, USA
E-mail: kcr@creol.ucf.edu
I. Martin, Dr. T. J. Prosa, Dr. D. J. Larson,[+] Dr. H. Francois-Saint-Cyr
AMETEK Materials Analysis Division
CAMECA Instruments Inc.
Madison, WI 53711, USA
E-mail: hugues.fsc@thermofisher.com
Dr. S. Antonov
Department Microstructure Physics and Alloy Design
Max-Planck-Institut für Eisenforschung GmbH
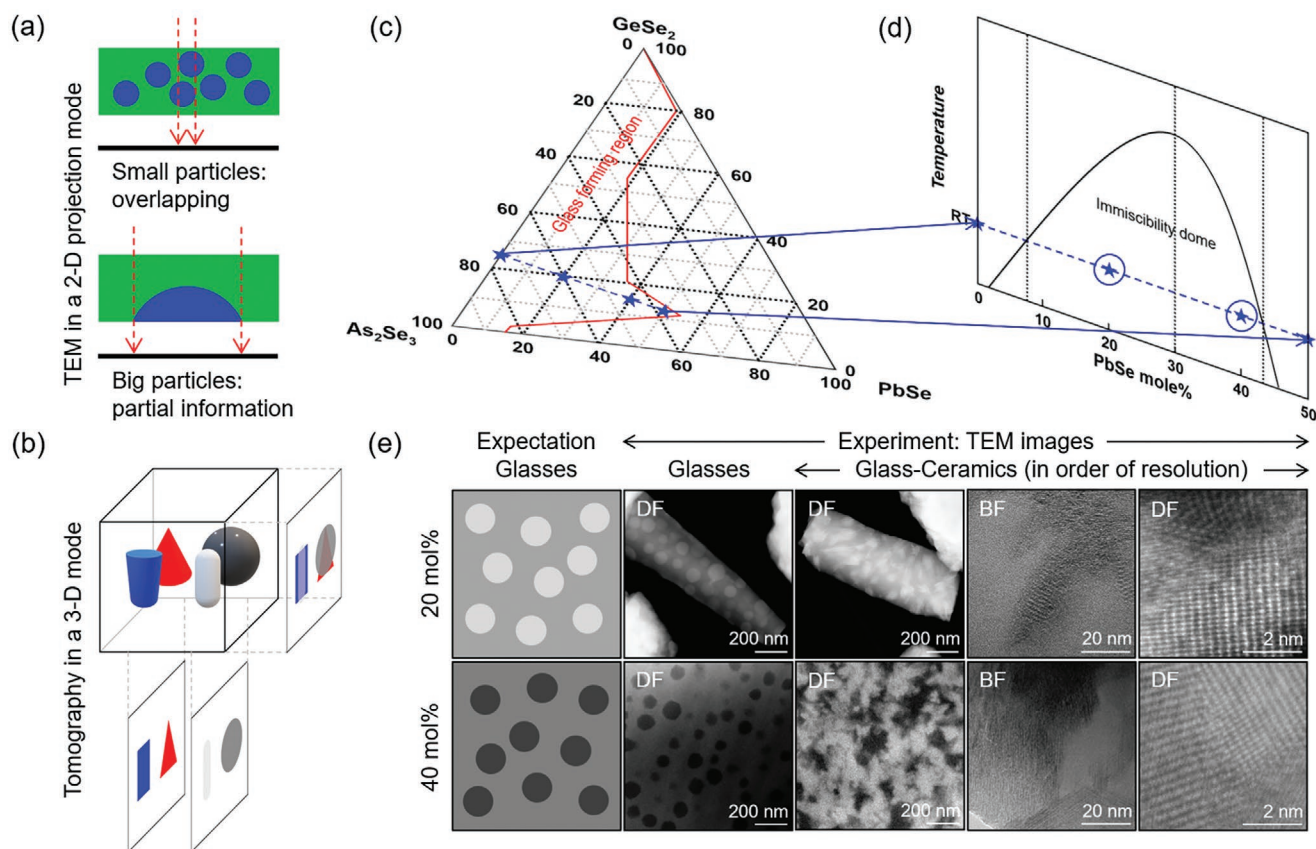Düsseldorf 40237, Germany

Figure 1. TEM-based analysis and microstructural map. a) TEM's limitations associated with its 2D projection. b) The visual concept of tomography enabling the identification of constituents in a 3D space. c) The horizontal triangle is GeSe$_2$-As$_2$Se$_3$-PbSe glass' ternary compositional diagram at room temperature. The red solid line corresponds to a compositional boundary between amorphous and crystalline regions at room temperature. The blue dotted tie line corresponds to a constant GeSe$_2$:3As$_2$Se$_3$ ratio with varying PbSe content within the glass forming region. d) The vertical parallelogram represents a plot of temperature versus composition of the glass along the tie line. The blue stars in both (c) and (d) represent compositions which exhibit key morphologies within and outside the immiscibility dome. e) Expected microstructures and experimental TEM images in compositional and thermal process windows. DF and BF correspond to dark field and bright field, respectively. Figure 1e adapted with permission.[18] Copyright 2020, Wiley-VCH.

an effective medium with a gradient in both effective refractive index and spectral dispersion.

Material synthesis methods now enable such gradients to be fabricated in bulk and thin film chalcogenide materials, but metrology tools required to quantify the variation in morphology, chemistry, and optical function in a 3D space have lagged behind this processing know-how. Specifically, chalcogenide glass and glass-ceramic nanocomposites have been characterized in our prior efforts exclusively using transmission electron microscopy (TEM) to reveal their microstructure.[17–21] Since cross-sectional TEM specimens are thin slabs of thickness less than 50 nm to be electron-transparent, the technique provides a specimen's microstructure from a 2D projection perspective. Thus, TEM has an intrinsic limitation in identifying how coexisting phases in a nanocomposite medium such as the Ge-As-Pb-Se system are distributed in a 3D space, as illustrated in **Figure 1a**. Specifically, for one of coexisting phases smaller than the thickness of a cross-sectional TEM specimen of the nanocomposite, the electron beam penetrates both the phases thereby collecting an integrated signal coming from the two phases. For one

of coexisting phases larger than the thickness of the cross-sectional TEM specimen, the phase seen in TEM images are sliced views of a portion of the feature, omitting key morphological information. Therefore, 2D TEM data used to assess microstructure in optical composites often fail to provide critical information including the type, size, shape, connectivity, and chemistry of the coexisting phases in the third, axial direction. Such information is critical to the design and fabrication of true 3D optical composites with tailored microstructures. In parallel, estimates of effective media properties and performance based on quantified volume fractions of varying phases and their respective properties have fallen short in these materials where only 2D mapping of microstructure was possible. Therefore, it is crucial to have a complimentary experimental metrology method which allows identification of the critical geometric, chemical, and spectral information in a 3D space since the information has a significant impact on the behavior of incident electromagnetic waves travelling through the optical nanocomposite medium.

Atom probe tomography (APT), pioneered by Panitz and commercialized with substantial instrumental refinements over

few decades,[22–27] has been demonstrated to be an increasingly promising microscopy technique, providing a 3D reconstruction of constituent elements' spatial distribution from a specimen of interest, as illustrated in Figure 1b. Importantly, materials traditionally considered outside the realm of APT such as chalcogenides with poor electrical conductivity have recently entered the avenue of the technique. Notable examples include Ge-S,[28] Ge-Sb-Te,[29] Ge-Te,[29] Pb-Te,[30] and Sb-Te.[31] This significant advance is primarily due to the introduction of pulsed lasers into APT analysis whereby laser thermal pulsing of a target material's evaporation rate significantly alleviates issues associated with the sample's electrical behavior.[27] While APT has been previously introduced to some of the chalcogenide family, the substantially irradiation sensitive and excessively fast milling Ge-As-Pb-Se material with coexisting phases exhibiting largely different evaporation fields studied here is the epitome of all challenges appearing in one place pushing the APT to the extreme. Therefore, in addition to the technical suitability and advantage of the metrology method, the development of a specimen preparation procedure and analytical parameters to acquire good results with the atom probe for this material system would help further bring this still-challenging chalcogenide family to the mainstream target for APT, thereby marking a milestone in paving the way toward the tehcnique's previously unconventional area.

Hence, we herein utilize APT to observe the microstructure of $GeSe_2$-As_2Se_3-PbSe nanocomposite glasses system and their evolution into glass-ceramics upon heat treatment in a 3D space. The spatial and temporal information quantified by the first-ever APT-assisted characterization of these chalcogenide nanocomposites was then inserted as input parameters into an optical calculation to predict the effective media's key optical performance metrics including transmittance, refractive index dispersion, and Abbe number. Their noticeably closer match with experimental data, as compared to those using TEM, suggests that the APT-assisted characterization greatly refines the structure–property relationship of this material system, thereby providing accurate feedback toward the realization of GRIN materials which can deliver advanced optical functions for current and next generation imaging systems in a single component.

2. Results and Discussion

Figure 1c shows the horizontal plane which corresponds to the glass' ternary compositional diagram at room temperature.[18,19] The diagram is divided by the red solid line into glass-forming and spontaneously/randomly crystallized regions following a quenching of a melted compound. Since one of keys to the realization of GRIN media is the ability to spatially control the formation of high refractive index crystalline phases, the amorphous region is required for a starting material where heat treatment or laser exposure can induce such nanocrystallites in a spatially tunable fashion. Within the amorphous region, the dotted blue tie line of a constant $GeSe_2$:$3As_2Se_3$ ratio with varying PbSe content [i.e., $(GeSe_2\text{-}3As_2Se_3)_{1-x}PbSe_x$] indicates the composition alloying available within a subsection of the amorphous region.

While a starting material with a composition along the tie line is amorphous, it exhibits a composition-dependent morphological variation. Pb integrated into the glass network of this material system does not disperse homogeneously, thereby inducing the glass to be phase-separated into Pb-rich and Pb-deficient phases over a specific range of PbSe content. Specifically, Figure 1d shows the vertical plane which represents a plot of temperature versus composition of the glass along the tie line where an immiscibility dome has been reported to exist for PbSe content ranging from ≈5–10 to ≈40–45 mol% at room temperature.[18,19] The immiscibility dome indicates that an increase in PbSe content would involve morphological transitions from a homogeneous medium (0–≈10 mol%) to Pb-rich particles in a Pb-deficient matrix (≈10–≈30 mol%) to Pb-deficient particles in a Pb-rich matrix (≈30–≈45 mol%) back to a homogeneous medium (≈ 45–50 mol%). The blue stars in Figure 1c,d correspond to compositions including 0, 20, 40, and 50 mol%, which represent such four regimes.

Here, glass nanocomposites with 20 and 40 mol% PbSe (i.e., $20GeSe_2$-$60As_2Se_3$-20PbSe and $15GeSe_2$-$45As_2Se_3$-40PbSe, respectively) are of particular importance in both microstructural and optical perspectives for following reasons: The Pb-rich phases are energetically unstable, making them prone to crystallization at a temperature lower than that typically required for the Pb-deficient phase. Specifically, crystalline phases are formed exclusively within the Pb-rich particles (matrix) in glasses with 20 (40) mol% PbSe while the Pb-deficient phase remains amorphous upon heat treatment. X-ray diffraction measurements in our previous studies indicate that the glass-ceramic nanocomposites with 20 mol% PbSe have two types of crystalline phases including As_2Se_3 and $Ge_{0.1}Pb_{0.9}Se$ with their volume fractions of 13.356% and 5.442% while those with 40 mol% PbSe have three types of crystalline phases including As_2Se_3, PbSe, and Se with their volume fractions of 14.068%, 10.451%, and 3.517%, respectively.[18,19] While these crystalline phases are too small to directly measure their refractive indices using conventional optical metrologies, we expect true values to be similar to those of their bulk form unless the size-dependent quantum effect begins to play for particles with a size below ≈10 nm which is not a case in our study. The refractive indices of bulk As_2Se_3, $Ge_{0.1}Pb_{0.9}Se$, PbSe, and Se crystals at a wavelength of 4.5 µm in the mid-wave IR (MWIR) as an example are 2.41, 4.81, 4.90, and 2.65, respectively. Here, it is important to note that the MWIR refractive indices of Pb-containing crystalline phases such as $Ge_{0.1}Pb_{0.9}Se$ and PbSe are far greater than those (≈2.9–3.1) of the starting glass nanocomposites, thereby playing a key role in increasing the effective refractive index of a glass-ceramic nanocomposite resulting upon heat treatment. Since the crystallization occurs exclusively within Pb-rich phases, the size of resulting crystallites is dictated by that of Pb-rich phases in starting glasses. The sizes typically ranging from ≈50 to 250 nm are substantially smaller than the wavelength of IR waves, allowing them to remain sub-wavelength upon heat treatment and making the nanocomposite a low-loss broadband transparent effective medium in the IR.[18,19]

The two illustrations in Figure 1e show inverse morphologies of glasses with the two compositions of importance expected from their positions (highlighted with two blue circles) within the glass system's immiscibility dome in Figure 1d.[18,19] These
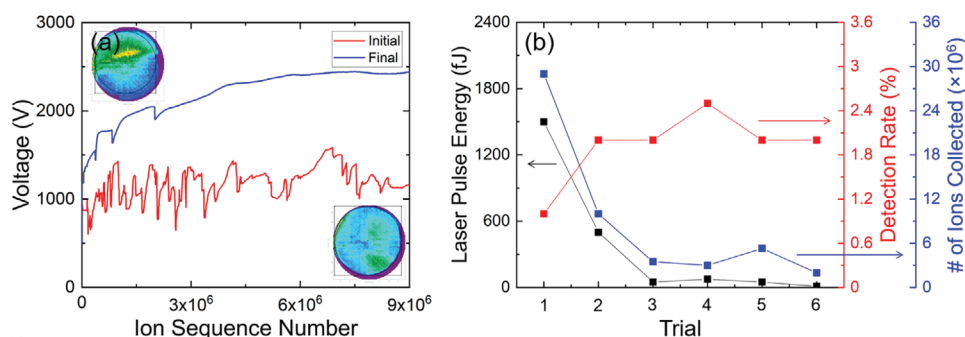
Figure 2. The optimization of APT signal collection parameters. a) The voltage histories as a function of ion sequence number and corresponding hit-maps for the glasses with 20 mol% PbSe, collected using initial unoptimized and final optimized signal collection parameters. b) The adjustment of laser pulse energy and resulting performance metrics such as detection rate and the number of ions collected.

morphologies are confirmed by TEM images exhibiting a particle-matrix structure where the circular shape of the particles suggests their amorphous phase.[18,19] Specifically, the brightness contrast associated with a difference in weight of constituent phases indicates that the particles and the matrix in the glass with 20 mol% PbSe are Pb-rich (heavy) and Pb-deficient (light), respectively, while being vice versa in the glass with 40 mol% PbSe. Upon heat treatment, the phases in starting glasses transform to have asymmetric shapes and the high-resolution images clearly show that the crystalline fringes exist exclusively within the dark regions in the bright field (BF) TEM images, strongly indicating the selective crystallization of Pb-rich phases and the emergence of Pb-containing crystalline phases.

Chalcogenide nanocomposites as a new class of APT specimens necessitate the development of signal collection parameters due to their vastly different morphology and field evaporation response, inherent to the nature of the phases at play. Their evaporation behaviors and corresponding challenges are closely associated with the anatomy of APT's signal collection process. Specifically, at the first order, the electric field (F) at the tip surface is directly related to the applied voltage (V) and is inversely proportional to the curvature radius (R) of the tip apex by $F = V/\beta R$ where β corresponds to a constant related to the shape of the specimen and the surrounding electrostatic environment.[23] A threshold electric field required to overcome the binding energy of a target specimen and eject constituent ions is quantified as an evaporation field. This means that, for the ion field evaporation to statistically occur, a specific voltage, translated in an electric field, needs to be provided to a specimen. For a tip of multiphased material with alternating increasing and decreasing evaporation fields, the applied voltage needs to be correspondingly adjusted to prevent an exceedingly rapid removal of a phase with a low evaporation field and avoid a complete fracture of the tip.

The large difference in evaporation fields of coexisting phases often makes such adjustment very challenging. When a phase with a much lower evaporation field undergoes a high electric field suitable for coexisting phases with greater evaporation fields, an excessively large number of ions are ejected, leaving a microfracture at the apex of a tip, and arrive at a detector. The applied voltage responds to the number of ions arriving at the detector and due to the sudden arrival of such a large number

of ions, the voltage instantaneously drops to relevel to an initially targeted detection rate. This effect appears as a succession of bursts in the plot of voltage versus ion sequence number (i.e., voltage history) and signals a transition from a phase to another one on a hit-map. The red voltage history and one of its corresponding hit-maps produced during the course of signal detection in **Figure 2a** show an example of such effect observed from glasses with 20 mol% PbSe. Furthermore, the material's overall excessively fast milling rate often leads to the generation of molecular complex ions, rather than individual elemental ones, which are responsible for additional peaks in a resulting mass spectrum. Therefore, both the highly phase-separated morphology and the fast-milling nature of the material, characterized as bursts in a voltage history and the complexity of a mass spectrum, makes the accurate spatial collection of constituent elements very challenging.

Here, a key to the alleviation of the issues can be gleaned by understanding roles of the DC voltage and voltage pulses which constitute the total voltage applied on the apex of a tip. The electric field is fed by the voltage given in a DC mode with an addition of voltage pulses.[26] The pulsed field evaporation generated by voltage pulses allows the flight time of each ejected ion to be measured and used to calculate the mass-to-charge ratio, thereby determining its chemical identity.[26] Meanwhile, to induce pulsed field evaporation using voltage pulses, specimen must have high electrical conductivity, limiting the technique to metals and highly doped semiconductors. Alternatively, sub-nanosecond laser pulses have been used to generate a pulse in the field evaporation rate for any target materials independent of their electrical conductivity.[26] Here, the pulsed voltage is substituted by the laser pulse energy (LPE). Lowering LPE has been reported to minimize the occurrence of molecular complex ions as well as issues associated with a large difference in evaporation fields of coexisting phases. However, adjusting LPE comes with its own issues. Since the curvature radius of a tip increases during the field evaporation, the applied voltage needs to be gradually increased to keep the electric field at the evolving tip surface constant, thereby still allowing the statistical evaporation of ions from a tip.[23] When lowering LPE, the DC voltage needs to be accordingly adjusted (increased) to reach the corresponding total voltage. An increase in DC voltage then makes a specimen prone to fracture. Therefore, the trade-off between the roles of LPE and DC voltage needs to
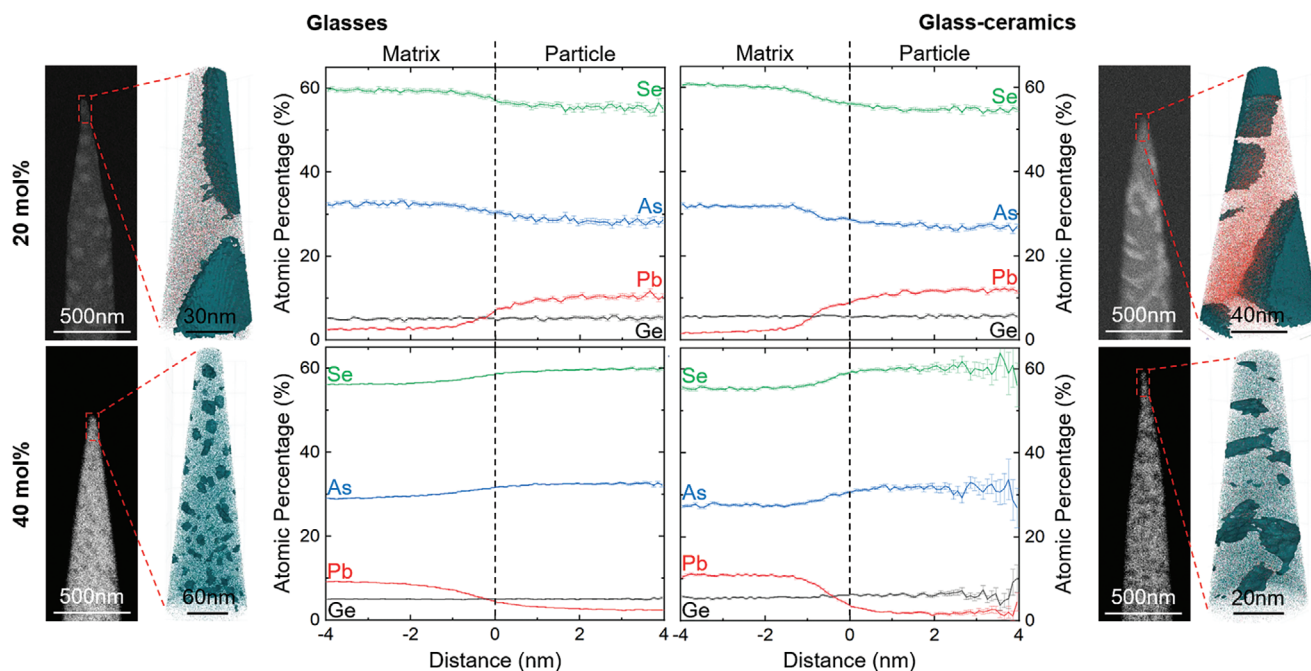
Figure 3. FIB images of APT tips, 3D isoconcentration surface maps of tips, spatial atomic percentage profiles of constituent elements for glasses and glass-ceramics with 20 and 40 mol% PbSe. The statistical variation of data along multiple lines crossing particle–matrix interfaces is shown as error bars. Adapted with permission.[32] Copyright 2020, Cambridge University Press.

be considered to balance the two parameters, thereby alleviating issues originated from the highly phase separated morphology and the fast-milling nature of the material while securing a tip.

Based upon this strategy, we optimized our protocol by incrementally lowering LPE and correspondingly increasing the DC voltage while monitoring the shape of tips to a point where the number of bursts in a voltage history was reduced, resulting in fewer observed molecular complex ions in a resulting mass spectrum and tips that remain structurally intact. The blue voltage history line with only three bursts in Figure 2a illustrates the result of the parameter optimization as compared to data in red with a succession of bursts. Figure 2b shows the history of LPE attempted and resulting performance metrics including the detection rate and the number of ions collected. Evidently, lowering LPE, within a range which avoids side effects associated with increasing DC voltage, enables maintaining reasonable performance metrics sufficient to have statistically meaningful set of data. This is evidenced by an excellent mass resolving power of >1000 of the mass spectrum which allows corresponding elemental and compound ions to be clearly identified, as discussed in the Supporting Information.

Figure 3 shows focused ion beam (FIB) images of APT tips of glasses and glass-ceramics with 20 and 40 mol% PbSe, reconstructed 3D ion maps of the tips (see the Supporting Information for their rotational views), and atomic percentages of constituent elements across a particle–matrix interface in each tip. The FIB images of APT tips of both glasses with 20 and 40 mol% PbSe readily exhibit circular particles embedded in a matrix while having inverse bright contrasts between the two regions, indicating compositional variations across particle–matrix interfaces in an opposite fashion. In the 3D ion maps,

regions where the atomic percentage of Pb is 5% are visualized as isoconcentration surfaces which are effectively interfaces between particles and a matrix. Atomic percentages of four constituent elements, extracted over a distance across an isoconcentration surface, clearly show that particles and a matrix are Pb-rich (deficient) and Pb-deficient (rich) in glasses with 20 (40) mol% PbSe, respectively, consistent with those identified using TEM. While exhibiting similar inverse bright contrasts in FIB images of tips and spatial distributions of constituent elements, glass-ceramics develop facets at their particle–matrix interfaces, indicating the presence of crystallites which emerge as a consequence of heat treatment.

Further insight into the phase separation in glasses, the morphological evolution upon heat treatment, and key difference in information extracted using APT and TEM are revealed by quantitative comparisons of plots in Figure 3. **Figure 4a** compares atomic percentages of four constituent elements across particle–matrix interfaces in APT tips of glasses with 20 and 40 mol% PbSe where those of Pb are magnified in Figure 4b. The overlay shows that the increase in PbSe content from 20 to 40 mol% in glasses leads to a decrease in the extent of phase separation. The fact that the glass with 40 mol% PbSe has a greater total of Pb while exhibiting a lesser segregation of Pb within the Pb-rich phase indicates that the region would have a volume fraction much higher than that of Pb-rich particles in the glass with 20 mol% PbSe to make sense of its total amount. This indication is confirmed by the set of data for the glass with 40 mol% PbSe in Figure 4B where Pb-rich region is identified as a matrix. Figure 4c,d shows the same set of data extracted from APT tips of a glass and a glass-ceramic with 20 mol% PbSe. While long-distance atomic migration is
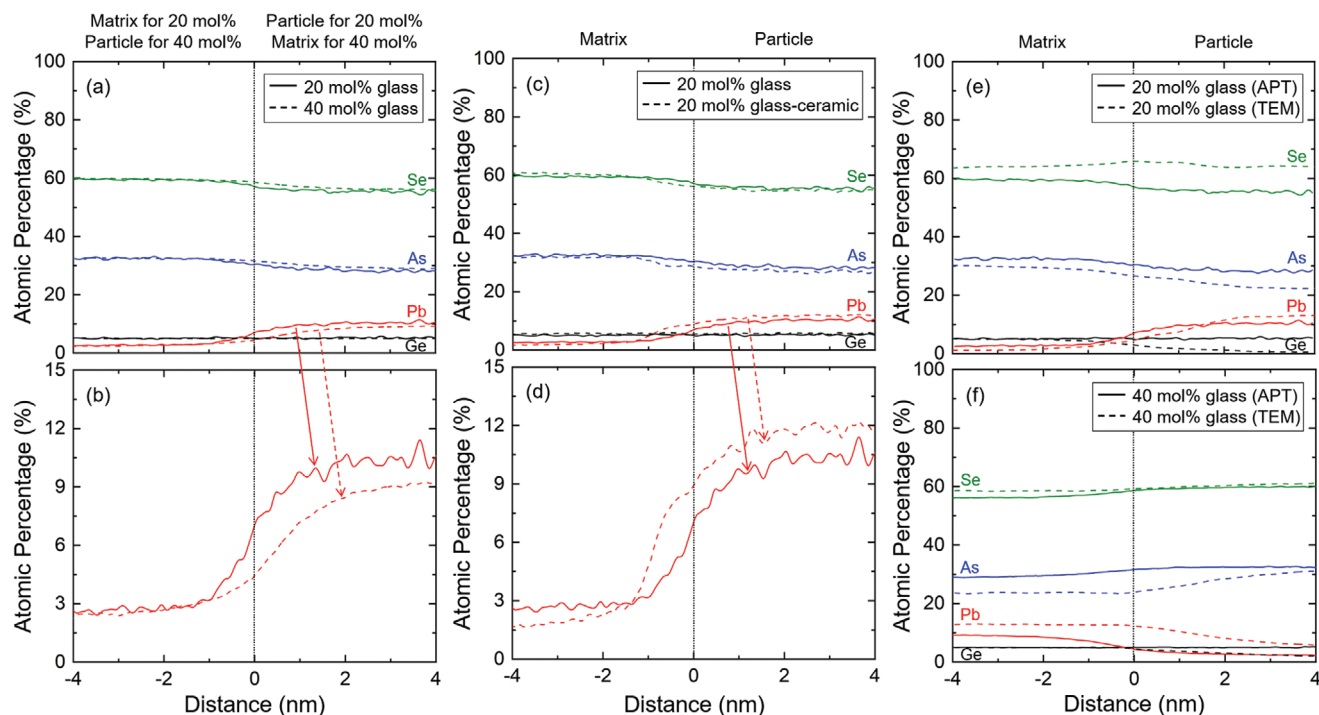
ADVANCED
SCIENCE NEWS
www.advancedsciencenews.com

ADVANCED
OPTICAL
MATERIALS
www.advopticalmat.de

Figure 4. Quantitative comparisons of constituent elements' average spatial atomic percentage profiles across compositional, thermal process, and instrumental method windows. a) Spatial atomic percentage profiles of elements for glasses with 20 and 40 mol% PbSe extracted using APT. b) Magnified profiles of Pb in (a). c) Spatial atomic percentage profiles of elements for a glass and a glass-ceramic with 20 mol% PbSe extracted using APT. d) Magnified profiles of Pb in (c). e) Spatial atomic percentage profiles of elements for glasses with 20 mol% PbSe extracted using APT and TEM. f) Spatial atomic percentage profiles of elements for glasses with 40 mol% PbSe extracted using APT and TEM.

not likely during a heat treatment, the close-view of Pb's spatial profiles in Figure 4d shows that further segregation occurs over a short distance during the process. The uphill diffusion of Pb from a nearby matrix to particles likely occurs while the crystallization of Pb-rich compounds is underway to lower the total energy of the system and reach an energetically stable state.

Glasses with 20 and 40 mol% PbSe are taken as examples to highlight key compositional differences extracted using APT and TEM (Figure 4e,f). Specifically, while the atomic percentage of Se appears to be spatially uniform across a particle–matrix interface based on TEM analyses, APT-extracted data show that the element is depleted in particles (a matrix) of glasses with 20 (40) mol% PbSe. The instrument-associated compositional difference observed for Se applies to Ge in an opposite fashion. The TEM-extracted data suggests that there is a spatial segregation of Ge while APT clarifies that the element is uniformly distributed. Both APT and TEM analyses show that particles and a matrix are Pb-rich (deficient) and Pb-deficient (rich) in glasses with 20 (40)mol% PbSe while being *vice versa* for As. Meanwhile, the APT analysis reveals that both the extent of the segregation and the values of their atomic percentages are noticeably different from those extracted using TEM.

Key attributes to desirable GRIN lenses include broadband IR transparency, refractive index tailorability, and minimized chromatic aberration, necessitating an ability to accurately predict the three metrics in optical design and material fabrication. Here, we assess the robustness and advantage of the APT-driven prediction over that using TEM. **Figure 5a** shows the

transmittance (i.e., internal transmission) spectrum of the glass with 20 mol% PbSe. The spectrum was converted from a raw transmission data of disk specimens with 10 mm diameter and 2 mm thickness where a refractive index dispersion was used to remove a Fresnel reflection-induced optical loss. Internal optical losses in chalcogenide nanocomposites originate intrinsically from the scattering of incident electromagnetic wave at the interfaces between coexisting phases and extrinsically from impurities imparted into the solid. The scattering-induced intrinsic optical loss in our glass leads to a rapid drop in intensity of its transmittance at a short-wave region of $\lambda \approx 1$–1.5 μm. The extent and spectral trend of scattering is determined by the size, shape, connectivity, volume fraction, and composition of coexisting phases as well as their refractive index. Meanwhile, impurities responsible for the extrinsic optical loss include O, C, and H which are typically bonded to constituent atoms and exist as functional groups.[33,34] Specifically, there are four noticeable absorption bands located at wavelengths of 2.91, 6.35, 8.27, and 13.26 μm in our transmittance spectrum. These bands are attributed to OH^- (2.91 μm), H_2O (6.35 μm), and As_4O_6 (8.27 and 13.26 μm) groups.[33,34] While these impurities can be removed by purification methods, no purification of elemental starting materials was carried out in this study. We have utilized a Zemax-assisted scattering model where geometric and chemical parameters extracted using APT and TEM, along with the refractive index of coexisting phases, were inserted as input parameters to calculate short-wave ($\lambda = 1.0$ and 1.5 μm) IR transmittance (T), reflectance (R),
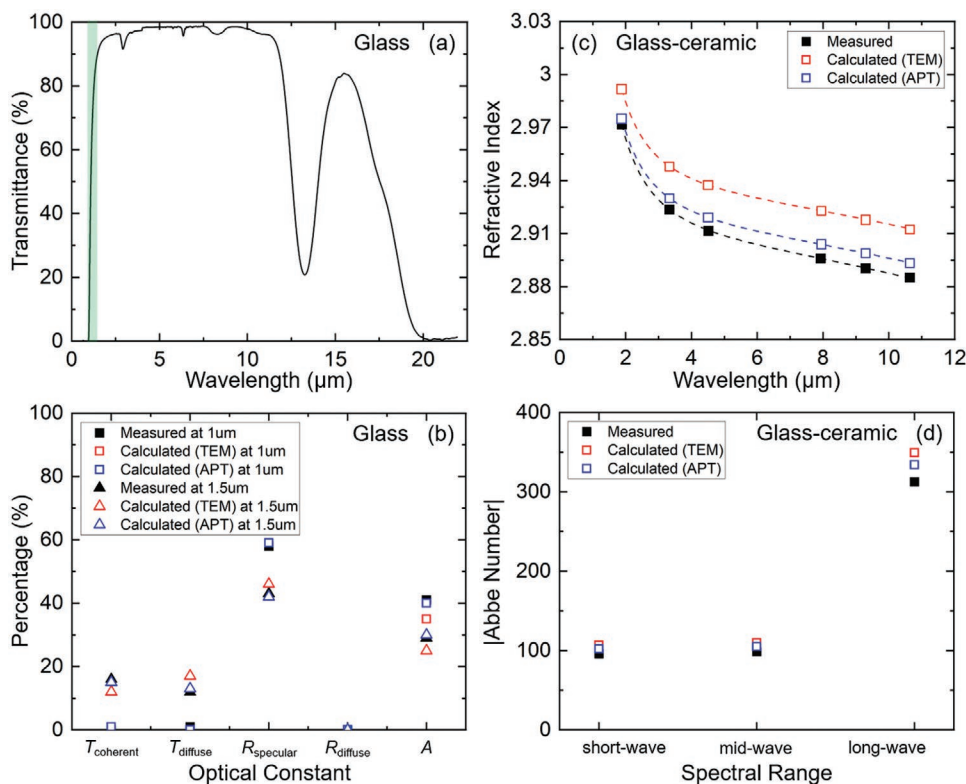
Figure 5. a) The glass' transmittance spectrum where its optical loss in the short-wave IR (SWIR) is highlighted. b) Calculated transmittance, scattering, reflectance, and absorption of the glass based on parameters extracted using APT and TEM as compared to experimental data. c) Calculated refractive index dispersion of the glass-ceramic based on parameters extracted using APT and TEM as compared to experimentally measured data. d) The magnitude of SWIR, MWIR, and long-wave IR Abbe numbers of the glass-ceramic extracted using the three refractive index dispersions in (c). Measurement errors are smaller than the size of data points. The magnitudes of both measured and calculated optical quantities in (b), (c), and (d) are less than the size of symbols.

and absorption (A) of the glass with 20 mol% PbSe. Figure 5b shows the calculated values as compared to experimental data where the optical constants calculated using APT are noticeably closer to the measured values, indicating parametric accuracy enabled by APT.

Such trend is similarly observed for calculated refractive index dispersion and Abbe number data. A glass-ceramic nanocomposite's effective refractive index can be approximated by knowledge of the refractive indices of a residual amorphous phase and induced crystalline phases as well as their respective volume fractions; $n_{\text{effective}} \approx V_{\text{amorphous phase}} \times n_{\text{amorphous phase}} +$

$\sum_{i=1}^{N} (V_{i_{\text{th}} \text{ crystalline phase}} \times n_{i_{\text{th}} \text{ crystalline phase}})$ where n and V correspond

to refractive index and volume fraction of the nanocomposite's phases, respectively.[18,19] Figure 5c shows calculated and measured effective refractive indices of the glass-ceramic with 20 mol% PbSe at six wavelengths across the IR, all of which are fitted with a Sellmeir function (dotted lines) to generate their refractive index dispersions. Evidently, APT-driven prediction shows a much closer match with the measured data across the entire spectral region, as compared to that calculated using TEM.

In addition to the extent of the computed refractive indices' deviation from that measured at each wavelength, how such

deviation varies across the spectral range, translated into how the dispersive nature of their refractive index spectra differs, is of importance for potential use of the material as an optical component. This is critical in designing the optical system where color correction relies on a pair of optical elements and thus is as important as any gradient in refractive index of the medium. The Abbe number is the measure of this dispersion, calculated from index data within a defined spectral window of

use as $V = \dfrac{n_{\text{center}} - 1}{n_{\text{short}} - n_{\text{long}}}$ where n_{short}, n_{center}, and n_{long} are the

refractive indices of a material at three different wavelengths of interest. The extent of material dispersion which dictates resulting chromatic aberration, decreases as the absolute value of the Abbe number increases. This is illustrated for a broad range of commercial optical glasses in the SCHOTT glass chart.[35] Here, the refractive index dispersions fitted from the calculated and measured data in Figure 5c were used to

extract the magnitude of short-wave $\left(\dfrac{n_{2.0\mu m} - 1}{n_{1.6\mu m} - n_{2.4\mu m}} \right)$, mid-

wave $\left(\dfrac{n_{4\mu m} - 1}{n_{3\mu m} - n_{5\mu m}} \right)$, and long-wave $\left(\dfrac{n_{10\mu m} - 1}{n_{8\mu m} - n_{12\mu m}} \right)$ IR Abbe

numbers for the three distinct spectral regions, as shown in Figure 5d. Consistently, the APT-assisted extraction exhibits a

better accuracy over that enabled using TEM in predicting Abbe number in three spectral ranges. While not fully optimized in the data analysis realm, the superb agreement points to APT as a viable means for characterizing multiphase optical material systems and presents a pathway toward composition/microstructure optimization to facilitate tailorable optical composites for diverse applications not currently satisfied with conventional homogeneous glasses or crystalline media.

While the APT characterization of nanocomposite materials greatly alleviates issues associated with TEM's 2D projection perspective and enables the calculation of optical constants closely matching experimental data as demonstrated in this study, the predicted values still exhibit deviations from measured data. Here, we discuss remaining issues associated with the discrepancy and suggestions for near future work applicable for a wide range of nanocomposite materials.

First, sample preparation based on Ga^+ FIB could potentially change their microstructures. The issue is likely to be pronounced for irradiation-sensitive chalcogenide nanocomposite material examined in this study. Alternatively, Xe^+ plasma-FIB systems utilize inert Xe gas as the milling agent. The chemically inert Xe gas has a low reactivity with the vast majority of elements and is expected to minimize undesirable secondary ion–matter interactions beyond milling within target materials which are sensitive to other types of ions.[4] Reportedly, Xe^+ plasma-FIB induces less damage and thinner amorphous surface layer to target specimens as compared to those imparted by Ga^+ source.[36] We foresee that by employing sample preparation based on Xe^+ plasma-FIB, defect-free/minimized APT specimens of the chalcogenide glasses and glass-ceramics can be fabricated, revealing further insight on the true microstructure of the nanocomposites.

Second, while refractive indices of crystalline phases induced upon heat treatment are known, it is challenging to identify that of a residual amorphous phase due to its size far smaller than a minimum measurement spot. Therefore, the index of the amorphous phase, while expected to change upon heat treatment due to its compositional evolution is just approximated to be same as the effective index of a starting glass nanocomposite for convenience in this study. Meanwhile, the molar refractivity calculation, which takes into account the atomic percentage of constituent elements within a specific region of interest, is expected to tackle the challenge. Furthermore, we have estimated the effective index of a nanocomposite via simple volumetric averaging of indices related to amorphous and crystalline phases. While this approach provides a rough estimate, it is important to note that the accurate estimation of a nanocomposite's effective refractive index requires the understanding of coexisting phases' chemical bond structures in addition to their compositions and geometries. Specifically, a difference in the dielectric strengths of coexisting phases, along with their compositions and geometries, is necessary to accurately estimate the polarization responses of coexisting phases and correspondingly that of a whole nanocomposite. This necessitates a more rigorous analytical solution such as anisotropic Maxwell Garnett solutions along with the discrete dipole approximation where an ensemble of microscopic dipoles dictated by the factors which encompass the geometry, composition, and chemical bond structure of coexisting phases

is modeled to accurately predict the effective behavior of a nanocomposite.[37]

3. Conclusion

In conclusion, a highly sought-after chalcogenide $GeSe_2$-As_2Se_3-PbSe glass and glass-ceramic nanocomposites served as the testbed optical material to demonstrate that state-of-the-art APT can overcome limitations of TEM's 2D projection perspective to yield critical microstructural information in a 3D space. Data from experimentally determined microstructural mapping in a 3D space allowed us to deterministically predict optical constants such as transmittance, refractive index, and Abbe number, which match experimentally measured data substantially closer than those calculated using TEM. Our study links processing and characterization methods to extend the information realized in 2D to 3D, providing a key attribute to the establishment of this novel material system's quantitative process–structure–property relationship. The predictive relationship strengthens a method to accurately and efficiently identify its optical properties and accordingly design its fabrication process parameters to yield composites with properties needed to demonstrate specific target optical functions. Furthermore, the correlative toolbox, enabling optical designers to benefit from quantitative input appropriate for use in the prediction of optical properties, is expected to be applicable to a wide variety of optical composite material systems.

4. Experimental Section

Glass Fabrication and Heat Treatment: Bulk glasses and glass-ceramics with compositions of $20GeSe_2$-$60As_2Se_3$-20PbSe and $15GeSe_2$-$45As_2Se_3$-40PbSe were melted and quenched from elemental materials in small 40 g batches. The resulting 10 mm diameter rods of glass were then annealed and sliced into approximately 2 mm thick disks. These disks were double-sided polished with a PR Hoffman double-sided lapping machine (PR-2) with a 5 μm slurry. Final surfaces were hand polished with a 0.05 μm slurry. Heat treatment steps were carried out in a muffle furnace (ThermoScientific 48000) in air atmosphere calibrated with a type K thermocouple. The nucleation temperature was set to be the glass transition temperature of each glass type and the growth temperature was set to the peak of the first crystallization peak of each glass' composition. The heat treatment times were constant, with nucleation steps performed for an hour and growth steps for 30 min. Samples were isothermally treated by placing them inside the furnace after the furnace was at the targeted temperature for nominally 30 min.

APT Specimen Preparation and Data Collection: FIB milling was performed on the bulk glass and glass-ceramic samples to prepare APT specimens of a needle shape with <100 nm tip radius using FEI Helios 660 FIB Dual Beam. The APT data collection and analysis were carried out using a CAMECA LEAP 5000XR. A set of optimal process conditions was identified, including the deposition of a sacrificial Ni layer prior to the FIB milling as well as low base temperature of 30 K, high detection rate of 2%, low pulse frequency of 50–100 kHz driven by the automated pulse control, and extremely low laser pulse energy of 10–50 fJ for the APT data collection.

TEM Specimen Preparation and Data Collection: Cross-sectional specimens with a width of 10 μm and a depth of 8 μm were prepared

ADVANCED
SCIENCE NEWS
www.advancedsciencenews.com

ADVANCED
OPTICAL
MATERIALS
www.advopticalmat.de

by focused ion beam milling followed by lift-out processing in a FEI 200TEM FIB. The specimens were then mounted on Cu grids and ion polished to ≈50 nm in thickness to be electron transparent. TEM imaging and selected area electron diffraction were carried out in a FEI Tecnai F30 TEM with an electron beam acceleration voltage of 80 kV.

Optical Measurements: The room temperature refractive indices were measured at six wavelengths across the IR including 1.88, 3.3, 4.515, 7.968, 9.294, and 10.717 µm, using a Metricon prism coupler that was modified for use in the IR. The experimental uncertainty of the measurement was typically on the order of 10^{-4} refractive index units. The discrete indices were fitted with a Sellmeier function $\left(n = \sqrt{A + \dfrac{B\lambda^2}{\lambda^2 - C^2} + \dfrac{D\lambda^2}{\lambda^2 - E^2}}\right)$ where Abbe numbers in the short-wave (1.6–2.4 µm), mid-wave (3–5 µm), and long-wave (8–12 µm) IR regions were extracted. For transmittance, reflectance, and absorption measurements, it was begun with the energy conservation equation of $100\% = T_{total} + R_{total} + A = T_{coherent} + T_{diffuse} + R_{specular} + R_{diffuse} + A$. First, $T_{coherent}$ was measured using FTIR and UV–vis spectrometers (ThermoFisher Nicolet iS5 FTIR and CARY 500 UV–vis). Second, both $T_{diffuse}$ and R_{total} were measured using an integrating sphere. Third, $R_{diffuse}$ was obtained by subtracting $R_{specular}$ from R_{total} where $R_{specular}$ is equal to $R\dfrac{1 + (1 - 2R)e^{-2\alpha_T d}}{1 - R^2 e^{-2\alpha_T d}}$. Fourth, $R_{specular}$ was calculated from the attenuation coefficient, α_T, obtained from the transmittance equation of $T_{coherent} = \dfrac{(1 - R^2)e^{-\alpha_T d}}{1 - R^2 e^{-2\alpha_T d}}$, where the surface reflection, R, is extracted from the effective refractive index and d corresponds to the thickness of a specimen. Lastly, A was extracted from the energy balance (i.e., $A = 100\% - T_{total} - R_{total}$).

Optical Calculations: A scattering model similar in concept to the integrating sphere setup was created in Zemax which takes into account parameters including sample thickness, index dispersion, Rayleigh scattering length, and bulk absorption. Since the average sizes of co existing phases in the chalcogenide nanocomposites are orders of magnitude smaller than incident IR electromagnetic wave, the Rayleigh-scattering model was employed. The scattering efficiency and its phase function (i.e., the angular distribution of the scattered light) are formulated by $Q_s = \dfrac{128\pi^4 a^4}{3\lambda^4}\left|\dfrac{n_s^2 - n^2}{n_s^2 + 2n^2}\right|$ and $p(\theta) = \dfrac{3}{16\pi}(1 + \cos^2\theta)$, respectively, where a is the radius of scattering phases, λ is the wavelength of incident electromagnetic wave in a vacuum, n_s is the refractive index of scattering phases, n is the refractive index of a medium, and θ is the scattering angle. The scattering and absorption parameters were adjusted until a match with results from the integrating sphere measurement was obtained for T_{total}, R_{total}, and A.

Supporting Information

Supporting Information is available from the Wiley Online Library or from the author.

Acknowledgements

Conflict of Interest

The authors declare no conflict of interest.

Data Availability Statement

Research data are not shared.

[1] X. H. Zhang, Y. Guimond, Y. Bellec, *J. Non-Cryst. Solids* **2003**, *326*, 519.
[2] D. H. Cha, H. Kim, Y. Hwang, J. C. Jeong, J. Kim, *Appl. Opt.* **2012**, *51*, 5649.
[3] H. Hisakuni, K. Tanaka, *Opt. Lett.* **1995**, *20*, 958.
[4] S. Ramachandran, J. C. Pepper, D. J. Brady, S. G. Bishop, *J. Lightwave Technol.* **1997**, *15*, 1371.
[5] G. Beadie, W. S. Rabinovich, J. Sanghera, I. Aggarwal, *Opt. Commun.* **1998**, *152*, 215.
[6] A. Saitoh, K. Tanaka, *Appl. Phys. Lett.* **2003**, *84*, 1725.
[7] E. A. Sanchez, M. Waldmann, C. B. Arnold, *Appl. Opt.* **1974**, *2011*, 50.
[8] Y. Kumaresan, A. Rammohan, P. K. Dwivedi, A. Sharma, *ACS Appl. Mater. Interfaces* **2013**, *5*, 7094.
[9] M. J. Booth, *Light: Sci. Appl.* **2014**, *3*, e165.
[10] D. T. Moore, *Appl. Opt.* **1980**, *19*, 1035.
[11] H. H. Li, *J. Phys. Chem. Ref. Data* **1980**, *9*, 561.
[12] G. Zuccarello, D. Scribner, R. Sands, L. J. Buckley, *Adv. Mater.* **2002**, *14*, 1261.
[13] R. A. Flynn, E. F. Fleet, G. Beadie, J. S. Shirk, *Opt. Express* **2013**, *21*, 4970.
[14] D. Gibson, S. Bayya, V. Nguyen, J. Sanghera, M. Kotov, G. Drake, *Proc. SPIE* **2015**, *9451*, 94511P-1.
[15] F. Bociort, *J. Opt. Soc. Am. A* **1996**, *13*, 1277.
[16] P. K. Manhart, R. Blankenbecler, *Opt. Eng.* **1997**, *36*, 1607.
[17] K. Richardson, M. Kang, L. Sisken, A. Yadav, S. Novak, A. Lepicard, I. Martin, H. Francois-Saint-Cyr, C. M. Schwarz, T. S. Mayer, C. Rivero-Baleine, A. J. Yee, I. Mingareev, *Opt. Eng.* **2020**, *59*, 1.
[18] M. Kang, L. Sisken, C. Lonergan, A. Buff, A. Yadav, C. Goncalves, C. Blanco, P. Wachtel, J. D. Musgraves, A. V. Pogrebnyakov, E. Baleine, C. Rivero-Baleine, T. S. Mayer, C. G. Pantano, K. A. Richardson, *Adv. Opt. Mater.* **2020**, *8*, 20000150.
[19] L. Sisken, M. Kang, J. M. Veras, C. Smith, A. Buff, A. Yadav, D. McClane, C. Blanco, C. Rivero-Baleine, T. S. Mayer, K. Richardson, *Adv. Funct. Mater.* **2019**, *29*, 1902217.
[20] M. Kang, A. M. Swisher, A. V. Pogrebnyanov, L. Liu, A. Kirk, S. Aiken, L. Sisken, C. Lonergan, J. Cook, T. Malendevych, F. Kompan, I. Divliansky, L. B. Glebov, M. C. Richardson, C. Rivero-Baleine, C. G. Pantano, T. S. Mayer, K. Richardson, *Adv. Mater.* **2018**, *30*, 1803628.
[21] I. Mingareev, M. Kang, M. Truman, J. Qin, G. Yin, J. Hu, C. M. Schwarz, I. B. Murray, M. C. Richardson, K. A. Richardson, *Opt. Laser Technol.* **2020**, *126*, 106058.
[22] J. A. Panitz, *Rev. Sci. Instrum.* **1973**, *44*, 1034.
[23] D. J. Larson, T. J. Prosa, R. M. Ulfig, B. P. Geiser, T. F. Kelly, *Local Electrode Atom Probe Tomography*, Springer, New York **2013**.
[24] T. F. Kelly, D. J. Larson, *Annu. Rev. Mater. Res.* **2012**, *42*, 1.
[25] J. Bunton, D. Lenz, J. Olson, K. Thompson, R. Ulfig, D. Larson, T. Kelly, *Microsc. Microanal.* **2006**, *12*, 1730.
[26] A. Cerezo, P. H. Clifton, M. J. Galtrey, C. J. Humphreys, T. F. Kelly, D. J. Larson, S. Lozano-Perez, E. A. Marquis, R. A. Oliver, G. Sha, K. Thompson, M. Zandbergen, R. L. Alvis, *Mater. Today* **2007**, *10*, 36.
[27] G. L. Kellogg, T. T. Tsong, *J. Appl. Phys.* **1980**, *51*, 1184.
[28] J. Orava, Y. Wen, J. Prikry, T. Wagner, N. A. Stelmashenko, M. Chen, A. L. Greer, *J. Mater. Sci.: Mater. Electron.* **2017**, *28*, 6846.

[29] M. Zhu, O. Cojocaru-Miredin, A. M. Mio, J. Keutgen, M. Kupers, Y. Yu, J.-Y. Cho, R. Dronskowski, M. Wuttig, *Adv. Mater.* **2018**, *30*, 1706735.

[30] Y. Yu, S. Zhang, A. M. Mio, B. Gault, A. Sheskin, C. Scheu, D. Raabe, F. Zu, M. Wuttig, U. Amouyal, O. Cojocaru-Miredin, *ACS Appl. Mater. Interface* **2018**, *10*, 3609.

[31] M. Zhu, W. Song, P. M. Konze, T. Li, B. Gault, X. Chen, J. Shen, S. Lv, Z. Song, M. Wuttig, R. Dronskowski, *Nat. Commun.* **2019**, *10*, 3525.

[32] M. Kang, H. Francois-Saint-Cyr, I. Martin, R. Sharma, C. Blanco, S. Antonov, T. J. Prosa, K. A. Richardson, *Microsc. Microanal.* **2020**, *26*, 3078.

[33] A. Yadav, M. Kang, C. Smith, J. Lonergan, A. Buff, L. Sisken, K. Chamma, C. Blanco, J. Caraccio, T. Mayer, C. Rivero-Baleine, K. Richardson, *Phys. Chem. Glasses* **2017**, *58*, 115.

[34] A. Yadav, M. Kang, C. Goncalves, C. Blanco, R. Sharma, K. Richardson, *Opt. Mater. Express* **2020**, *10*, 2274.

[35] Interactive Abbe Diagram, https://www.us.schott.com/advanced_optics/english/knowledge-center/technical-articles-and-tools/abbe-diagramm.html (accessed: January 2021).

[36] J. Liu, R. Niu, J. Gu, M. Cabral, M. Song, X. Liao, *Sci. Rep.* **2020**, *10*, 10324.

[37] V. A. Markel, *J. Opt. Soc. Am. A* **2016**, *33*, 1244.